# Compensating hysteresis and mechanical misalignment in piezo-stepper actuators

van Meer, Max; van Meijel, Tim; van Halsema, Emile; Verschueren, Edwin; Witvoet, Gert; Oomen, Tom

**DOI**
10.1016/j.mechatronics.2025.103394

**Publication date**
2025

**Document Version**
Final published version

**Published in**
Mechatronics

Mechatronics 111 (2025) 103394

Contents lists available at ScienceDirect

Mechatronics

journal homepage: www.elsevier.com/locate/mechatronics

# Compensating hysteresis and mechanical misalignment in piezo-stepper actuators☆,☆☆

Max van Meer [a,*], Tim van Meijel [a], Emile van Halsema [b], Edwin Verschueren [b], Gert Witvoet [a,c], Tom Oomen [a,d]

[a] Department of Mechanical Engineering, Control Systems Technology, Eindhoven University of Technology, Eindhoven, PO Box 513, 5600MB, The Netherlands
[b] Thermo Fisher Scientific, Eindhoven, The Netherlands
[c] Department of Optomechatronics, TNO, Delft, The Netherlands
[d] Delft Center for Systems and Control, Delft University of Technology, Delft, The Netherlands

ARTICLE INFO

*Keywords:*
Piezo actuators
Feedforward control
Hysteresis
Iterative learning control

ABSTRACT

Piezo-stepper actuators enable accurate positioning through the sequential contraction and expansion of piezoelectric elements, generating a walking motion. The aim of this paper is to reduce velocity ripples caused by parasitic effects, due to hysteresis in the piezoelectric material and mechanical misalignments, through suitable feedforward control. The presented approach involves the integration of a rate-dependent hysteresis model with a position-dependent feedforward learning scheme to compensate for these effects. Experimental results show that this approach leads to a significant reduction in the velocity ripples, even when the target velocity is changed. These results enable the use of piezo-stepper actuators in applications requiring high positioning accuracy and stiffness over a long stroke, without requiring expensive position sensors for high-gain feedback.

## 1. Introduction

Piezo-stepper actuators offer a promising solution for nano-scale positioning by combining high stiffness, a long stroke, and precise motion control. High stiffness minimizes deformation under load, while a long stroke extends their applicability to tasks requiring significant range of motion [1–3]. These features make them well-suited for applications such as scanning tunneling microscopy (STM) and electron microscopy (EM) [4–6].

Multiple piezo-stepper designs are available for different purposes. For EM and STM, the design relies on an ingenious stacking of piezoelectric elements, see Fig. 1. Clamp elements expand vertically to press shear elements onto a central mover, while the shear elements expand laterally to displace the mover. When the shears reach the end of their stroke, the clamps disengage, allowing a second set of clamps and shears to take over, generating a walking motion over a large stroke. Fig. 2 illustrates the idealized reference displacements for the individual piezo elements during this process.

The stacking of piezo elements introduces a number of parasitic effects that must be compensated in high-accuracy applications: hysteresis and mechanical misalignments. Hysteresis, an inherent property of piezoelectric materials, leads to a history-dependent relationship between the applied voltage and the resulting displacement. Mechanical misalignments, on the other hand, arise due to manufacturing and assembly tolerances, causing the piezo elements to expand or retract in unintended directions. When left unaddressed, these misalignments result in velocity ripples of the mover (see Fig. 3). Both effects significantly impact positioning performance and must be addressed to be applicable in high-accuracy applications.

Existing solutions to mechanical misalignments have achieved notable improvements in performance. Position feedback control suppresses velocity ripples [7], improving accuracy while retaining flexibility. Model-based optimization of voltage waveforms [8] further improves stepping performance. Data-driven feedforward methods, such as Iterative Learning Control (ILC) [9], refine reference displacements using measured position data, achieving nearly constant velocity [10,

☆ This work is part of the research program VIDI with project number 15698, which is (partly) financed by The Netherlands Organisation for Scientific Research (NWO). In addition, this research has received funding from the ECSEL Joint Undertaking under grant agreement 101007311 (IMOCO4.E). The Joint Undertaking receives support from the European Union's Horizon 2020 research and innovation program.
☆☆ This paper was recommended for publication by Associate Editor Toru Namerikawa.
* Corresponding author.
*E-mail address:* m.v.meer@tue.nl (M. van Meer).

https://doi.org/10.1016/j.mechatronics.2025.103394
Received 14 March 2025; Received in revised form 20 June 2025; Accepted 27 July 2025
Available online 13 August 2025

11]. Despite these achievements, existing solutions introduce critical limitations. Feedback control requires high bandwidth over an additional, possibly expensive, position sensor to be effective, amplifying noise and limiting suitability for nano-scale positioning [12]. Model-based approaches require costly parameter identification, and ILC-based methods compensate for hysteresis when not explicitly addressed, resulting in history-dependent references that reduce task flexibility.

Hysteresis compensation methods have also shown progress in improving positioning accuracy. Operator-based models, such as the Prandtl–Ishlinskii and Preisach models, capture the nonlinear, history-dependent behavior of hysteresis and are widely used in feedforward control [13–16]. Recent research extends these operator-based models with rate-dependent formulations that take dynamic hysteresis effects into account [17,18]. Differential-based models, including Bouc-Wen, Dahl, and Duhem models [19,20], as well as observer-based approaches [21] and direct inverse hysteresis modeling [22,23], have also proven effective. Piezo displacement measurements, required for hysteresis modeling, can even successfully be estimated from measurements of the current, reducing component costs [24,25]. Despite their strengths, these methods face challenges when applied to feedforward control. Operator-based models are computationally expensive, complicating real-time control, while differential-based models are difficult to identify reliably due to non-convexity [26,27]. Direct inverse modeling, although avoiding inversion steps, complicates validation against experimental data. Data-driven feedforward approaches, including observer-based methods, often rely on piezo element displacement measurements, which are impractical in applications with limited space or cost constraints. While piezo displacement estimation from measurements of currents has proven useful for feedback control, literature on its application to hysteresis feedforward is sparse.

Although significant progress has been made in improving the performance of piezo-stepper actuators, no existing method compensates for both mechanical misalignments and hysteresis without amplifying noise, requiring accurate models, limiting flexibility, or demanding high computational power. The aim of this paper is to develop a unified framework combining rate-dependent hysteresis compensation with data-driven learning for mechanical misalignments, relying solely on measurements of the piezo currents and mover position. The framework is designed for real-time hardware to achieve high positioning accuracy in industrial applications, and can be used in conjunction with feedback control. While the developed approach is demonstrated on a specific piezo-stepper actuator, the framework is general and can be applied to other piezo-stepper actuators with similar challenges.

The contributions of this paper are therefore as follows:

- C1 A rate-dependent hysteresis compensation method is developed that relies on measurements of the currents, eliminating the need for direct displacement sensors. The model uses few parameters and supports real-time implementation.
- C2 A data-driven approach is developed to address mechanical misalignments, incorporating iterative learning control to refine reference displacements. The learned compensation function is applicable to arbitrary reference motions.
- C3 These two methods are integrated into a unified feedforward control framework, ensuring high positioning accuracy across varying reference motions without requiring separate tuning per task.
- C4 The framework is experimentally validated on a piezo-stepper actuator, demonstrating its effectiveness in industrially relevant scenarios.

This paper is structured as follows. First, Section 2 formalizes the problem. Section 3 presents the rate-dependent hysteresis compensation method. Subsequently, Section 4 describes the compensation of mechanical misalignments and integrates both solutions into a unified framework. Section 5 presents experimental results, and Section 6 concludes the paper.

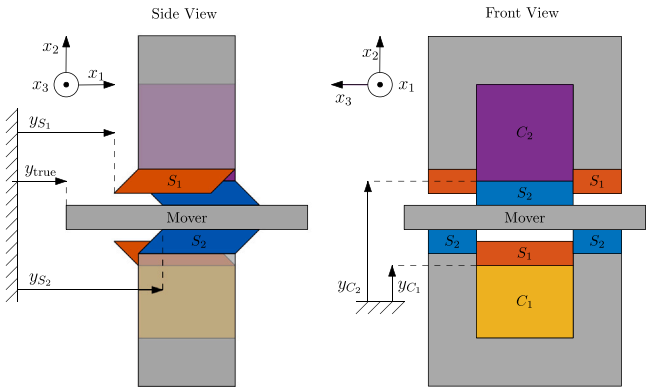


**Fig. 1.** Schematic of a piezo-stepper actuator. The clamps ($C_1$, $C_2$) press the shear elements ($S_1$, $S_2$) onto the mover. When a shear element $S_e$ is in contact with the mover, it expands or contracts laterally to push or pull the mover in the $x_1$ direction.

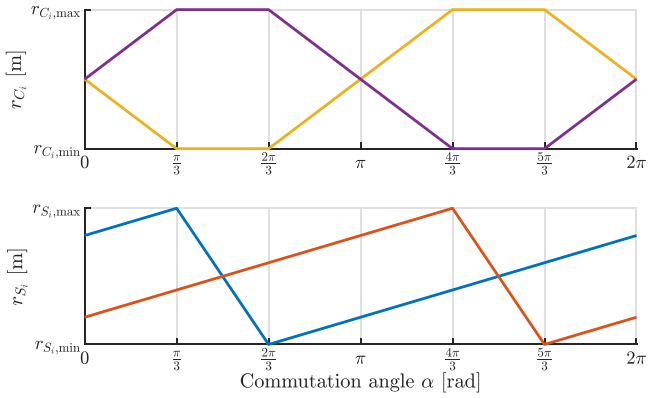


**Fig. 2.** Reference displacements for piezo elements to achieve a stepping motion. The clamps (—,—) press the shears (—,—) onto the mover one by one, and the shears drag the mover along in the lateral direction.

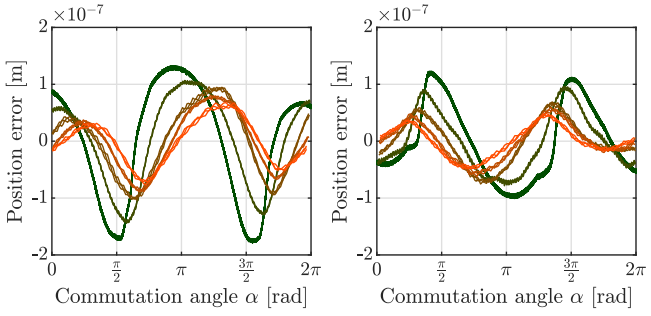


(a) Forwards stepping motion (b) Backwards stepping motion

**Fig. 3.** Position error of the mover against the commutation angle $\alpha$, using voltage waveforms that scale with the references in Fig. 2, for a range of constant drive frequencies between 0.4 Hz (—) and 100 Hz (—), showing three steps per frequency. The data shows a direction-dependent error that remains consistent across steps, suggesting it is caused by $\alpha$-domain disturbances. Variations across drive frequencies are attributed to a combination of history-dependent hysteresis effects and lowpass effects of the capacitive position sensor.

## 2. Problem formulation

This section describes the problem of accurate control of piezo-stepper actuators with task flexibility, starting with a description of the experimental setup that serves as a foundation for the problems addressed in this paper.

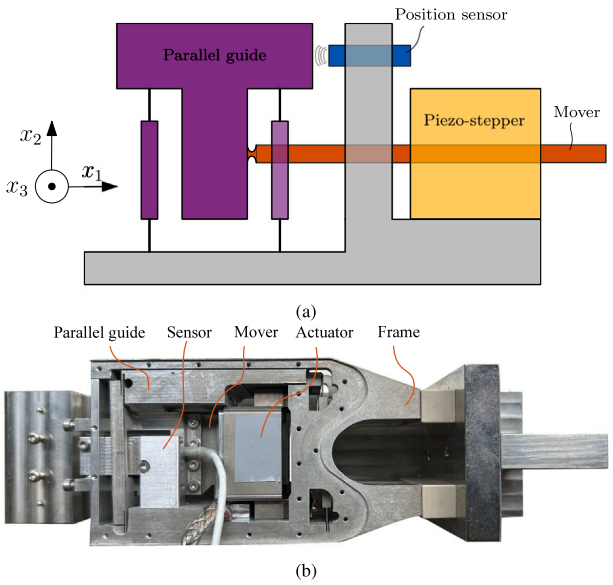


**Fig. 4.** Overview of the experimental setup. The lateral displacement $y$ of the mover is measured using a capacitive sensor via a parallel guide. The picture (b) shows a functionally identical prototype setup that uses an encoder instead of a capacitive sensor; the experimental results in this paper are based on the capacitive sensor setup.

### 2.1. Experimental setup

The experimental setup, shown in Fig. 4, consists of a piezo-stepper actuator provided by Thermo Fisher Scientific. The actuator achieves a range of 500 µm by stepping in intervals of up to 3 µm. The displacement $y$ of the mover is measured using a capacitive sensor with a sampling rate of 10 kHz.

The actuator operates via two groups of piezo elements, each containing a set of shear elements $(S_1, S_2)$ and a clamp element $(C_1, C_2)$. As shown in Fig. 1, the shears expand and contract laterally to move the central mover, while the clamps alternately press the shears onto the mover to enable a walking motion. The current through the piezo elements is recorded and available for offline estimation of the piezo displacements, as direct measurements of individual displacements are unavailable. This setup provides the platform for addressing the challenges of hysteresis and misalignments in piezo-stepper actuators.

### 2.2. Piezo element dynamics

The rate of displacement $\dot{y}_e(t)$ of a piezo element $e \in \Omega$ with $\Omega := \{S_1, S_2, C_1, C_2\}$, neglecting creep, is described by [13]:

$$\dot{y}_e(t) = M_e(\dot{u}_e(t), u_{e,a}(t))\dot{u}_e(t), \tag{1}$$

where $u_e(t)$ is the voltage applied to element $e$, $M_e$ is a hysteresis function, and $u_{e,a}(t)$ is the voltage absement, defined formally later. The absement captures voltage history in a single parameter, which has proven effective for modeling piezoelectric hysteresis [13]. The motion of the mover depends on the displacement of all piezo elements, as defined by:

$$\begin{aligned}
&\dot{y}_{\text{true}}(t) = \dot{y}^\circ(t) + \dot{d}(t),\\
&\dot{y}^\circ(t) := \kappa\left(\dot{y}_{S_1}(t), \dot{y}_{S_2}(t), \dot{y}_{C_1}(t), \dot{y}_{C_2}(t)\right)\\
&\kappa(\cdot) = \begin{cases}
\dot{y}_{S_1} & \text{if } y_{C_1} \geq y_{C_1,\text{c}} \text{ and } y_{C_2} < y_{C_2,\text{c}},\\
\dot{y}_{S_2} & \text{if } y_{C_2} \geq y_{C_2,\text{c}} \text{ and } y_{C_1} < y_{C_1,\text{c}},\\
\frac{1}{2}(\dot{y}_{S_1} + \dot{y}_{S_2}) & \text{if } y_{C_1} \geq y_{C_1,\text{c}} \text{ and } y_{C_2} \geq y_{C_2,\text{c}},\\
0 & \text{otherwise.}
\end{cases}
\end{aligned} \tag{2}$$

Here, $y_{C_i,\text{c}}$ are constants representing when clamps bring the shears into contact with the mover, and $\dot{d}(t)$ accounts for velocity disturbances such as slip and mechanical misalignments. The measured mover position, sampled at intervals $T_s = 1/F_s$, is expressed as:

$$y(t_k) = y(t_0) + G(q)\dot{y}_{\text{true}}(t_k), \tag{3}$$

where $q$ is the forward-shift operator in discrete-time such that $qt_k = t_{k+1}$ and $k$ is the sample number. The sensor $G(q)$ consists of a discrete-time integrator, a delay, and lowpass dynamics with a cutoff frequency around 100 Hz. Finally, it is assumed that $y(t_0) = \dot{y}(t_0) = 0$. The next section describes the problem of compensating the first parasitic effect, hysteresis.

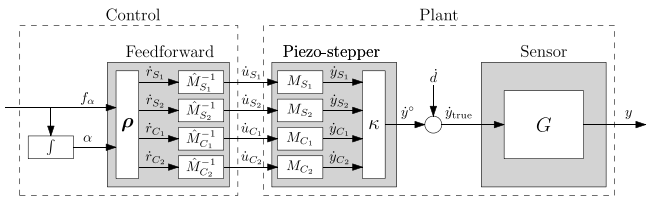


**Fig. 5.** Schematic depiction of feedforward control of a piezo-stepper actuator. The feedforward controller yields voltages based on a commutation angle $\alpha$. When applied to the piezo elements $e$, their individual motions $\dot{y}_e$ cause a displacement of the mover via kinematics $\kappa$. Mechanical misalignments in the piezo elements lead to a velocity disturbance $d$.

### 2.3. Hysteresis compensation

Piezo-stepper actuators exhibit hysteresis, causing a history-dependent relationship between voltage and displacement, see (1). To compensate for this, a model $\hat{M}_e$ approximates the true hysteresis function $M_e$ for every element and is inverted in a feedforward control law. When $\hat{M}_e \approx M_e$, the required voltages are given by

$$\dot{u}_e = \hat{M}_e^{-1}\dot{r}_e, \tag{4}$$

resulting in accurate tracking $\dot{y}_e \approx \dot{r}_e$ of the reference displacements. These reference displacements $\dot{r}_e$ are defined by a waveform function $\rho$ as

$$\begin{bmatrix}\dot{r}_{S_1} & \dot{r}_{S_2} & \dot{r}_{C_1} & \dot{r}_{C_2}\end{bmatrix}^\top = \rho(\alpha, f_\alpha), \tag{5}$$

where $\alpha \in [0, 2\pi)$ represents the commutation angle governing the relative progression through a step of the actuator. The angle $\alpha$ is determined by a user-defined drive frequency $f_\alpha(t)$ that specifies the number of steps per second:

$$\alpha(t) = \alpha(t_0) + 2\pi \bmod \left(\int_{t_0}^{t} f_\alpha(\tau)\mathrm{d}\tau, 1\right). \tag{6}$$

Fig. 5 illustrates this open-loop control scheme, where the feedforward controller determines the piezo voltages based on $\alpha$. The piezo elements then produce individual displacements, which collectively drive the mover through the kinematics $\kappa$. However, obtaining accurate hysteresis models $\hat{M}_e$ is challenging, as they must (*i*) be invertible, (*ii*) allow real-time evaluation at fast sampling rates, and (*iii*) correctly capture rate-dependent hysteresis effects. Any imperfections in the hysteresis model lead to a position error of the mover, degrading performance. The next section describes another parasitic effect that deteriorates positioning performance, which is not addressed by hysteresis compensation.

### 2.4. α-Dependent disturbances

The second parasitic effect arises from $\alpha$-dependent disturbances caused by slip and misalignments. Experimental data of the position error $\varepsilon(t_k) = r(t_k) - y(t_k)$ for a range of constant drive frequencies is

shown in Fig. 3. These experiments use simple reference displacements $\boldsymbol{\rho}(\alpha, f_\alpha)$, as displayed in Fig. 2, and a constant hysteresis model

$$\hat{M}_{e,\text{const}} = c_{M,e}, \quad \forall e \in \Omega, \quad c_{M,e} \in \mathbb{R}. \tag{7}$$

Fig. 3 demonstrates that the tracking error is consistent in the $\alpha$-domain across steps, significantly degrading positioning performance. This suggests that modifying $\boldsymbol{\rho}(\alpha, f_\alpha)$ could improve positioning accuracy, as $\boldsymbol{\rho}(\alpha, f_\alpha)$ governs the repeating motion of the piezoelectric elements. Variations over drive frequencies primarily result from lowpass effects of the capacitive sensor, as discussed in detail in Section 5. Moreover, the data indicates that the $\alpha$-dependent disturbances are direction-dependent, likely because a misalignment would cause a positive force in one direction, along the motion of the mover, but a negative force in the other direction, counteracting the motion.

### 2.5. Problem definition

The aim is to design a feedforward control law

$$u_e(t_k) = u_e(t_0) + f(r(t_k), \dots, r(t_0)), \quad \forall e \in \Omega \tag{8}$$

that minimizes the root-mean-square deviation (RMSD) of the mover position error $\varepsilon(t_k) = r(t_k) - y(t_k)$ for arbitrary reference signals $r(t_k)$, where the RMSD is given by

$$\varepsilon_{\text{RMSD}} = \sqrt{\frac{1}{N}\sum_{k=1}^{N}\left(\varepsilon(t_k) - \frac{1}{N}\sum_{k=1}^{N}\varepsilon(t_k)\right)^2}. \tag{9}$$

This measure quantifies the velocity ripples of the piezo-stepper actuator when the reference velocity is constant, but the formulation remains applicable to varying reference velocities as well. Two sub-problems are defined:

1. Hysteresis compensation: develop and invert hysteresis models $\hat{M}_e$ to ensure accurate tracking $\dot{y}_e \approx \dot{r}_e$ despite the absence of direct piezo displacement measurements.
2. Compensation of $\alpha$-domain disturbances: design $\boldsymbol{\rho}(\alpha, f_\alpha)$ to minimize $\varepsilon_{\text{RMSD}}$, independent of drive frequency $f_\alpha$, by leveraging mover position data $y$.

With effective feedforward compensation of hysteresis and $\alpha$-domain disturbances, the piezo dynamics become approximately linear. This enables the use of a linear feedback controller to suppress external vibrations and unmodeled effects by adjusting the drive frequency $f_\alpha(t_k)$ based on the error $\varepsilon(t_k)$. While feedback design is not addressed here, it is a straightforward extension, and the reduced disturbances allow for a low feedback bandwidth, improving robustness and minimizing sensor noise amplification.

The next section provides the solution to the first sub-problem, and Section 4 addresses the second sub-problem.

## 3. Rate-dependent hysteresis compensation

This section details the developed approach to rate-dependent hysteresis compensation in piezo elements.

### 3.1. Overview

First, an overview of the method is given, starting with a description of the control law governing the scheme in Fig. 5. To realize a desired movement $r_e$ of a single piezo element $e$, integration of (1) leads to

$$u_e(t) = u_e(t_0) + \int_{t_0}^{t} \frac{\dot{r}_e(\tau)}{M_e(\dot{u}_e(\tau), u_{e,a}(\tau))} d\tau, \tag{10}$$

where $u_e$ is the voltage required to achieve $y_e = r_e$, and $u_{e,a}(t)$ is the absement [13,28], which quantifies the accumulated voltage change since the last reversal:

$$u_{e,a}(t) := |u_e(t) - u_e(t_{\text{turn}})|, \quad t \geq t_{\text{turn}}, \tag{11}$$

with $t_{\text{turn}} = \max_\tau\{\tau < t : \dot{u}_e(\tau)\dot{u}_e(\tau+\epsilon) < 0\}$, where $\epsilon$ is an infinitesimally small positive number. Applying first-order discretization of (10) and introducing a delay in $\dot{u}_e(\tau)$ to avoid algebraic loops leads to the following control law:

$$u_e(t_k) = u_e(t_{k-1}) + \frac{T_s \dot{r}_e(t_{k-1})}{\hat{M}_{\theta_e}\left(\frac{|u_e(t_{k-1}) - u_e(t_{k-2})|}{T_s}, u_{e,a}(t_{k-1})\right)}, \quad k \geq 1, \tag{12}$$

where $\theta_e$ are the hysteresis model parameters, $u(t_k) = 0$ for $k \leq 0$, and $\dot{r}_e(t_k)$ is defined by (5). This control law comprises two contributions explained in the remainder of this section:

1. Identification of a hysteresis model: a model $\hat{M}_{\theta_e}$ is identified from measurements of the currents to approximate $M_e$, as explained in Section 3.2.
2. Implementation aspects: practical aspects of implementing the control law, such as a computationally efficient implementation and a solution to integrator drift, are addressed in Section 3.3.

### 3.2. Modeling rate-dependent hysteresis

The hysteresis function $M_e$ in (1) describes the relationship between piezo voltages and their displacements. While the voltages are known, being the control input, the individual piezo displacements are not measured directly. Instead, they are estimated from measurements of the current as follows. The rate of displacement of a piezoelectric element can be approximated [29] as

$$\dot{y}_e(t) \approx \xi_e i_e(t), \tag{13}$$

where $i_e$ is the measured current through element $e$ and $\xi_e$ is a constant in $\text{ms}^{-1}\text{A}^{-1}$. An estimate $\hat{\xi}_e \approx \xi_e$ for the shears is easily obtained using an offline experiment, by comparing data of the capacitive position sensor to the current measurements. The value is assumed identical for the clamps. Any mismatch $\hat{\xi}_e \neq \xi_e$ leads to a scaling of $\hat{M}_e$, but his mismatch is corrected for later, as detailed in Section 3.3.2.

Approximation (13) neglects time-varying external forces and dynamic effects, which may affect the accuracy of the estimated piezo displacement. To mitigate this, the actuator is loaded with a representative mass matching the intended application, and recalibration is recommended if the load changes significantly. Nonetheless, independent measurements from the capacitive position sensor confirm that this approximation has minimal impact during data collection, and experimental results in Section 5 show that the simplification does not noticeably decrease performance.

The key idea is to perform experiments with varying voltage signals to obtain measurements of

$$M_e(\dot{u}_e, u_{e,a}) = \left|\frac{\hat{\xi}_e i_e}{\dot{u}_e}\right|. \tag{14}$$

These measurements result in datasets

$$\mathcal{D}_e = \{\dot{u}_e(t_k), u_{e,a}(t_k), i_e(t_k)\}_{k=1}^{n}, \tag{15}$$

for all $e \in \Omega$. To account for direction-dependent hysteresis effects, separate models $\hat{M}_{\theta_{e^+}}$ and $\hat{M}_{\theta_{e^-}}$ are fit on this dataset, which are then used in the feedforward control law, such that

$$\hat{M}_{\theta_e} = \begin{cases} \hat{M}_{\theta_{e^+}} & \text{if } \dot{r}_e(t_k) \geq 0, \\ \hat{M}_{\theta_{e^-}} & \text{if } \dot{r}_e(t_k) < 0. \end{cases} \tag{16}$$

The next section explains the design of a single experiment that yields all datasets $\mathcal{D}_e$. Subsequently, the chosen model structure and fitting method are detailed.

**Algorithm 1** Data collection for hysteresis compensation

**Require:** Range $f_{\alpha,\min},\dots,f_{\alpha,\max}$ of $F$ application-relevant drive frequencies, number of steps $n_s$.
1: Initialize $\mathcal{D}_e = \{\}$ for all $e \in \Omega$, define $\mathcal{F}$ as in Eq. (17).
2: Start experiment with control law Eq. (12) using constant hysteresis model Eq. (7), $f_\alpha = 0$ and waveform function Eq. (18).
3: **for** $f_{\alpha,i} \in \mathcal{F}$ **do**
4: Update $f_\alpha \leftarrow f_{\alpha,i}$.
5: Wait for $t_{\text{step}} = \frac{n_s}{f_\alpha}$ seconds.
6: **end for**
7: Stop the experiment and store all $\left(\dot{u}_e(t_k), u_{e,a}(t_k), i_e(t_k)\right)$ in $\mathcal{D}_e$ for all $e \in \Omega$.
8: **return** Data-sets $\mathcal{D}_e$, $\forall e \in \Omega$.

#### 3.2.1. Experiment design

For the datasets $\mathcal{D}_e$ to be useful in modeling $\hat{M}_{\theta_{e^+}}$ and $\hat{M}_{\theta_{e^-}}$, the measured voltage pairs $(\dot{u}_e(t_k), u_{e,a}(t_k))$ should cover a range relevant to the application. Under control law (12) with some imperfect $\hat{M}_e$ and $\rho_e$ that achieve a stepping motion, albeit with parasitic effects, all pairs $(\dot{u}_e(t_k), u_{e,a}(t_k))$ depend solely on the chosen drive frequency $f_\alpha$. Therefore, a grid $\mathcal{F}$ of $F$ positive and negative drive frequencies in an application-relevant range between $f_{\alpha,\min}$ and $f_{\alpha,\max}$ is defined as

$$\mathcal{F} = \left\{ \pm f_{\alpha,i} \mid f_{\alpha,i} = f_{\alpha,\min}\left(\frac{f_{\alpha,\max}}{f_{\alpha,\min}}\right)^{\frac{i-1}{F-1}}, \quad i = 1,\dots,F \right\}, \tag{17}$$

where logarithmic spacing is used because of the potentially wide range of drive frequencies. Section 5 addresses the choice of $F$. An experiment is started where the drive frequency cycles stepwise through $\mathcal{F}$ for $n_s$ steps per frequency, with control law (12), using a constant hysteresis model (7) and the following nominal waveform function $\boldsymbol{\rho}(\alpha, f_\alpha)$ used in literature [10], defined as

$$\rho_{C_i}(\alpha, f_\alpha) = \begin{cases} |f_\alpha|\frac{r_{C_i,\max}-r_{C_i,\min}}{2\pi/3}(2i-3) & 0 \le \alpha < \frac{\pi}{3}, \\ 0 & \frac{\pi}{3} \le \alpha < \frac{2\pi}{3}, \\ -|f_\alpha|\frac{r_{C_i,\max}-r_{C_i,\min}}{2\pi/3}(2i-3) & \frac{2\pi}{3} \le \alpha < \frac{4\pi}{3}, \\ 0 & \frac{4\pi}{3} \le \alpha < \frac{5\pi}{3}, \\ |f_\alpha|\frac{r_{C_i,\max}-r_{C_i,\min}}{2\pi/3}(2i-3) & \frac{5\pi}{3} \le \alpha < 2\pi, \end{cases}$$

$$\rho_{S_1}(\alpha, f_\alpha) = \begin{cases} |f_\alpha|\frac{r_{S_1,\max}-r_{S_1,\min}}{5\pi/3} & 0 \le \alpha < \frac{\pi}{3}, \\ -|f_\alpha|\frac{r_{S_1,\max}-r_{S_1,\min}}{\pi/3} & \frac{\pi}{3} \le \alpha < \frac{2\pi}{3}, \\ |f_\alpha|\frac{r_{S_1,\max}-r_{S_1,\min}}{5\pi/3} & \frac{2\pi}{3} \le \alpha < 2\pi, \end{cases} \tag{18}$$

$$\rho_{S_2}(\alpha, f_\alpha) = \begin{cases} |f_\alpha|\frac{r_{S_2,\max}-r_{S_2,\min}}{5\pi/3} & 0 \le \alpha < \frac{4\pi}{3}, \\ -|f_\alpha|\frac{r_{S_2,\max}-r_{S_2,\min}}{\pi/3} & \frac{4\pi}{3} \le \alpha < \frac{5\pi}{3}, \\ |f_\alpha|\frac{r_{S_2,\max}-r_{S_2,\min}}{5\pi/3} & \frac{5\pi}{3} \le \alpha < 2\pi, \end{cases}$$

where $i \in \{1,2\}$ and $r_{e,\max}$, $r_{e,\min}$ define the maximum reference stroke of the elements. These reference displacements, depicted in Fig. 2, lead to similarly shaped voltage waveforms when scaled with a scalar $\hat{M}_{e,\text{const}}$ through control law (12). Hence, for every frequency $f_{\alpha,i} \in \mathcal{F}$, the measurements include data of one negative voltage rate, one positive voltage rate, and a range of different voltage absements. Algorithm 1 summarizes the data collection process, and the next section describes the hysteresis model structure.

#### 3.2.2. Model structure

To capture the rate-dependent hysteresis effects, the model structure must account for both the voltage rate $\dot{u}_e$ and the absement $u_{e,a}$. The Ramberg–Osgood model [30], which has proven successful in modeling hysteresis for fixed drive frequencies, does not include rate dependency [13]. Therefore, an alternative structure is presented that, like the Ramberg–Osgood model, is smooth in the voltage absement, but also allows for rate-dependency. The model is parametrized linearly in the parameters as

$$\hat{M}_{\theta_{e^\iota}}(\mathbf{x}_e) = \mathbf{k}^\top(\mathbf{x}_e)\boldsymbol{\theta}_{e^\iota}, \quad \iota \in \{+,-\}, \tag{19}$$

where the input vector is given by

$$\mathbf{x}_e := [|\dot{u}_e|, u_{e,a}]^\top. \tag{20}$$

Here, $\mathbf{k}(\mathbf{x}_e)$ is a vector of basis functions evaluated at the input $\mathbf{x}_e$, given by

$$\mathbf{k}(\mathbf{x}_e) = [k(\mathbf{x}_e, \mathbf{x}_{e,1}), \dots, k(\mathbf{x}_e, \mathbf{x}_{e,m})]^\top, \tag{21}$$

where $\mathbf{x}_{e,i}, i \in \{1,\dots,m\}$, are predefined grid points in $\mathbb{R}^2$, and $k : \mathbb{R}^2 \times \mathbb{R}^2 \to \mathbb{R}$ is a kernel function defining the structure of the model. To account for direction-dependent hysteresis effects, separate parameter vectors $\boldsymbol{\theta}_{e^+}$ and $\boldsymbol{\theta}_{e^-}$ are used for positive and negative velocity directions, see (16).

An example basis function that is useful in modeling functions when the nonlinear structure is smooth but not fully known, popularized by Gaussian Process regression [31], is given by

$$k(\mathbf{x}_e, \mathbf{x}'_e) = \sigma_f^2 \exp\left(-\frac{1}{2}\left(\mathbf{x}_e - \mathbf{x}'_e\right)^\top \boldsymbol{\Sigma}^{-1}\left(\mathbf{x}_e - \mathbf{x}'_e\right)\right). \tag{22}$$

Here, $\boldsymbol{\Sigma} = \text{diag}(\ell_1, \ell_2)$, $\ell_1, \ell_2 \in \mathbb{R}$ are tuning parameters that govern the smoothness of the basis functions in the direction of $\dot{u}_e$ and $u_{e,a}$, respectively. The parameter $\sigma_f^2$ scales the overall magnitude of the basis functions. A convenient choice is to set $\sigma_f^2$ to the sample variance of the observations of $M_e$. In this paper, parameters $\ell_{1,2}$ and $\sigma_f^2$ are tuned manually for a good fit to the data. Alternatively, this tuning process can be automated, e.g., by optimization of the marginal likelihood, as explained in [31]. Finally, to avoid the need to evaluate these kernel functions online, Section 3.3 presents a resource-efficient implementation.

#### 3.2.3. Obtaining the model

The parameters $\boldsymbol{\theta}_{e^\iota}$ in (19) are obtained by solving the following linear least-squares problem for each velocity direction $\iota \in \{+,-\}$:

$$\min_{\boldsymbol{\theta}_{e^\iota}} \|\mathbf{K}(\mathbf{X}_e^\iota)\boldsymbol{\theta}_{e^\iota} - \mathbf{m}_e^\iota\|_2^2, \tag{23}$$

where the data matrices are constructed separately for positive and negative velocity directions:

$$\mathbf{X}_e^+ = \{\mathbf{x}_e(t_k) \mid \dot{u}_e(t_k) \ge 0, \mathbf{x}_e(t_k), \dot{u}_e(t_k) \in \mathcal{D}_e\}, \tag{24a}$$

$$\mathbf{X}_e^- = \{\mathbf{x}_e(t_k) \mid \dot{u}_e(t_k) < 0, \mathbf{x}_e(t_k), \dot{u}_e(t_k) \in \mathcal{D}_e\}. \tag{24b}$$

The corresponding kernel matrices and measurement vectors are:

$$\mathbf{K}(\mathbf{X}_e^\iota) = \left[\mathbf{k}(\mathbf{x}_{e,1}^\iota), \dots, \mathbf{k}(\mathbf{x}_{e,n^\iota}^\iota)\right]^\top \in \mathbb{R}^{n^\iota \times m}, \tag{25}$$

$$\mathbf{m}_e^\iota = \left[\left|\frac{\hat{\xi}_e i_e(t_1)}{\dot{u}_e(t_1)}\right| \quad \dots \quad \left|\frac{\hat{\xi}_e i_e(t_{n^\iota})}{\dot{u}_e(t_{n^\iota})}\right|\right]^\top. \tag{26}$$

The least-squares solution for each direction is then given by

$$\hat{\boldsymbol{\theta}}_{e^\iota} = \left(\mathbf{K}^\top(\mathbf{X}_e^\iota)\mathbf{K}(\mathbf{X}_e^\iota)\right)^{-1}\mathbf{K}^\top(\mathbf{X}_e^\iota)\mathbf{m}_e^\iota. \tag{27}$$

This solution is valid as long as $\mathbf{K}^\top(\mathbf{X}_e^\iota)\mathbf{K}(\mathbf{X}_e^\iota)$ is full rank, which is typically satisfied since $m \ll n^\iota$.

Thus, the obtained model $\hat{M}_{\hat{\boldsymbol{\theta}}_e}$ captures rate-dependent and ui direction-dependent hysteresis effects and enables online compensation. The next section addresses implementation aspects.

### 3.3. Implementation aspects

This section covers some implementation aspects, starting with a resource-efficient implementation of the hysteresis model.

### 3.3.1. Resource-efficient implementation

The control law (12) requires the evaluation of the hysteresis model $\hat{M}_{\theta_{e^\iota}}$ at high sampling rates, which is computationally challenging because of the nonlinear terms in (22). Therefore, $\hat{M}_{\theta_{e^\iota}}$ is used to fill a lookup table $\hat{M}_{e^\iota}^{\mathrm{LUT}}(\mathbf{x}_e)$ offline. This renders the approach feasible for numerous embedded hardware platforms featuring large memory but limited computational capabilities, only requiring simple computations for linear interpolation:

$$\begin{aligned}\hat{M}_{e^\iota}^{\mathrm{LUT}}(\mathbf{x}_e) &= \begin{bmatrix}1-\tau_1 & \tau_1\end{bmatrix}\mathbf{Y}^\iota\begin{bmatrix}1-\tau_2\\ \tau_2\end{bmatrix},\\ \tau_1 &= \frac{x_1 - x_1^{(i)}}{x_1^{(i+1)} - x_1^{(i)}}, \quad \tau_2 = \frac{x_2 - x_2^{(j)}}{x_2^{(j+1)} - x_2^{(j)}},\\ \mathbf{Y}^\iota &= \begin{bmatrix}\hat{M}_{\theta_{e^\iota}}\left(\begin{bmatrix}x_1^{(i)}\\ x_2^{(j)}\end{bmatrix}\right) & \hat{M}_{\theta_{e^\iota}}\left(\begin{bmatrix}x_1^{(i)}\\ x_2^{(j+1)}\end{bmatrix}\right)\\ \hat{M}_{\theta_{e^\iota}}\left(\begin{bmatrix}x_1^{(i+1)}\\ x_2^{(j)}\end{bmatrix}\right) & \hat{M}_{\theta_{e^\iota}}\left(\begin{bmatrix}x_1^{(i+1)}\\ x_2^{(j+1)}\end{bmatrix}\right)\end{bmatrix}.\end{aligned} \tag{28}$$

Here, $(x_1^{(i)}, x_2^{(j)}, x_1^{(i+1)}, x_2^{(j+1)})$ are grid points surrounding $\mathbf{x}_e$, satisfying

$$x_1^{(i)} \le x_1 \le x_1^{(i+1)}, \quad x_2^{(j)} \le x_2 \le x_2^{(j+1)}, \tag{29}$$

and $\mathbf{Y}^\iota$ is computed offline for both $\iota \in \{+,-\}$. Since this method requires only several lookup-operations and linear interpolation between four points at every time-step, it is computationally cheaper than alternatives such as operator-based hysteresis compensation, which require many more operations [18,27]. The next section addresses the issue of integrator drift in the control law.

### 3.3.2. Integrator drift

While reference displacement rates (18) are zero-mean, the division of these references by rate-dependent hysteresis model $\hat{M}_e$ in (12) may lead to a voltage rate that is not zero-mean, leading to drift in the voltage $u_e$. In the worst case, this could lead to the clamps not fully extending to press the shears onto the mover, impairing stepping performance.

To mitigate the accumulation of this integrator drift over time, an anti-windup mechanism is introduced by constraining the output whenever the piezo voltages exceed user-defined bounds $u_{e,\min}$ and $u_{e,\max}$. These artificial bounds are defined for the purpose of drift compensation only and are stricter than the amplifier limits, i.e., $u_{e,\min} > u_{e,\min,\mathrm{amp}}$ and $u_{e,\max} < u_{e,\max,\mathrm{amp}}$. Hence, the final control law is given by

$$\begin{aligned}u_e(t_k) &= \begin{cases}u_{e,\min} & \text{if } \upsilon < u_{e,\min},\\ u_{e,\max} & \text{if } \upsilon > u_{e,\max},\\ \upsilon & \text{otherwise.}\end{cases}\\ \upsilon &= u_e(t_{k-1}) + \frac{T_s \dot{r}_e(\alpha(t_{k-1}))}{\hat{M}_e^{\mathrm{LUT}}\left(\left[\frac{|u_e(t_{k-1}) - u_e(t_{k-2})|}{T_s}, u_{e,a}(t_{k-1})\right]^\top\right)}.\end{aligned} \tag{30}$$

As long as the piezo voltages remain within the bounds $u_{e,\min}$ and $u_{e,\max}$, the drift compensation is inactive, and integrator drift can still occur, deteriorating stepping performance. On the other hand, when the bounds are reached, the control law saturates the output, preventing further drift but also limiting the achievable stroke. Therefore, it is desired that the voltage waveforms exceed the bounds at least once per cycle of the drive frequency. This condition is formally expressed as:

$$\begin{aligned}u_e(t_{\mathrm{top}}) &> u_{e,\max}, \quad \forall t_{\mathrm{top}} \in \mathcal{T}_{\mathrm{top}}(f_\alpha),\\ u_e(t_{\mathrm{bot}}) &< u_{e,\min}, \quad \forall t_{\mathrm{bot}} \in \mathcal{T}_{\mathrm{bot}}(f_\alpha),\end{aligned} \tag{31}$$

where the sets $\mathcal{T}_{\mathrm{top}}(f_\alpha)$ and $\mathcal{T}_{\mathrm{bot}}(f_\alpha)$ identify the time instances at which $u_e$ reaches its maximum and minimum values within one period $T = 1/f_\alpha$:

$$\begin{aligned}\mathcal{T}_{\mathrm{top}}(f_\alpha) &= \left\{t \in [0,T] : u_e(t) = \max_{t\in[0,T]} u_e(t)\right\},\\ \mathcal{T}_{\mathrm{bot}}(f_\alpha) &= \left\{t \in [0,T] : u_e(t) = \min_{t\in[0,T]} u_e(t)\right\}.\end{aligned} \tag{32}$$

This condition is satisfied by appropriate selection of reference strokes $r_{e,\max}$ and $r_{e,\min}$ in (18). These bounds are determined *offline* through optimization, once after Algorithm 1, ensuring that for each selected $f_\alpha$, the voltage $u_e(t)$ exceeds the artificial limits at least once per cycle. The optimization problem is given by

$$\begin{aligned}&\min_{r_{e,\max}, r_{e,\min}} J_{e,f_\alpha}(r_{e,\max}, r_{e,\min})\\ &\quad= \sum_{t_{\mathrm{top}}\in\mathcal{T}_{\mathrm{top},2}(f_\alpha)} \|u_e(t_{\mathrm{top}}) - u_{e,\max}\|_2^2\\ &\qquad+ \sum_{t_{\mathrm{bot}}\in\mathcal{T}_{\mathrm{bot},2}(f_\alpha)} \|u_e(t_{\mathrm{bot}}) - u_{e,\min}\|_2^2,\end{aligned} \tag{33}$$

subject to hysteresis model (19), waveforms (18), control law (30),

$$\begin{aligned}&\alpha(t_k) = 2\pi \mathrm{mod}\left(\alpha(t_{k-1}) + T_s f_\alpha\right), \quad \forall k \in \mathcal{K}_{\mathrm{sim}},\\ &u_e(t_0) = \alpha(t_0) = 0,\\ &\mathcal{T}_{(\cdot),2}(f_\alpha) = \mathcal{T}_{(\cdot)}(f_\alpha/2) \cap \{t \mid t \le 1/f_\alpha\}.\end{aligned}$$

Here, the simulated indices are $\mathcal{K}_{\mathrm{sim}} = \{1, \ldots, 2\lfloor F_s/f_\alpha \rfloor\}$, with flooring operator $\lfloor\cdot\rfloor$, consisting of two periods to account for transients. The problem is solved using interior-point optimization with approximate gradients [32].

The resulting optimal bounds $r_{e,\max}^\star$ and $r_{e,\min}^\star$ are precomputed for different drive frequencies and stored in lookup tables:

$$\begin{aligned}r_{e,\max}^\star &= g_{e,\max}^{\mathrm{LUT}}(f_\alpha),\\ r_{e,\min}^\star &= g_{e,\min}^{\mathrm{LUT}}(f_\alpha).\end{aligned} \tag{34}$$

The reference movements (18), combined with control law (30) and these optimized bounds, ensure continuous and repeatable motion of the mover despite hysteresis, while preventing drift due to modeling errors.

An advantageous side effect of optimizing the reference strokes is that it renders any mismatch $\hat{\xi}_e \neq \xi_e$ in (13) inconsequential. Indeed, such a mismatch results in a scaling error in $\hat{M}_e$, which affects the denominator in control law (30). However, since the reference strokes are optimized to achieve predefined voltage limits for this imperfect $\hat{M}_e$, affecting the numerator of (30), the scaling factors cancel out. The voltage waveforms are always scaled to the voltage limits $u_{e,\max}$ and $u_{e,\min}$ due to the cost function in (33).

## 4. Compensation of $\alpha$-dependent disturbances

The control law (30) enables accurate tracking of reference movements $\dot{r}_e(t)$ of individual piezo elements by compensating hysteresis, which is the first parasitic effect. The second parasitic effect, consisting of mechanical misalignments and slip, introduces velocity ripples that are repetitive in the $\alpha$-domain. This section introduces a data-driven approach to compensate for these $\alpha$-dependent disturbances, starting with an overview of the method.

### 4.1. Overview

The developed approach compensates for $\alpha$-domain disturbances by iteratively learning a compensation function that modifies the shear waveforms. These disturbances, shown in Fig. 3, are repetitive in the $\alpha$-domain and can therefore be mitigated effectively using Iterative Learning Control (ILC) [10]. Only the shear waveforms are modified as these directly affect the mover displacement through (2). The approach is summarized in Algorithm 2 and involves three contributions:

**Algorithm 2** Compensation of $\alpha$-domain disturbances

**Require:** Hysteresis models $\hat{M}_e^{\text{LUT}}$, $e \in \Omega$, functions $g_{e,\max}^{\text{LUT}}(f_\alpha), g_{e,\min}^{\text{LUT}}(f_\alpha)$, LTI model $\hat{G}(q)$, drive frequency $f_\alpha$.
1: Design filters $L(q)$, $Q(q)$, see Section 4.4.2.
2: Initialize $\boldsymbol{\gamma}_0 = \mathbf{0}$.
3: **for** $j \in [0, \dots, n_{\text{tr}} - 1]$ **do**
4: Conduct an experiment with control law Eq. (30), using reference Eq. (35). Store $y_j$.
5: Compute $\dot{f}_{j+1}(t_k)$ with Eq. (40).
6: Compute $\boldsymbol{\gamma}_{j+1}$ with Eq. (43).
7: **end for**
8: **return** the final compensation function $\dot{f}^{\text{proj}}_{\boldsymbol{\gamma}_{n_{\text{tr}}-1}}(\alpha)$.

1. A compensation function $\dot{f}^{\text{proj}}_{\boldsymbol{\gamma}}(\alpha)$ is parametrized to modify the shear waveforms. This function is updated iteratively using ILC to minimize the effects of $\alpha$-domain disturbances, as detailed in Section 4.2.
2. Monotonic convergence of Algorithm 2 is analyzed in Section 4.3.
3. Implementation aspects such as design of the learning filter and direction-dependency of the compensation function are described in Section 4.4.

In contrast to [10], the approach presented in this paper integrates compensation of $\alpha$-dependent disturbances with rate-dependent hysteresis compensation of all piezo elements, such that the learned compensation function is applicable to arbitrary drive frequencies and does not require relearning when the task changes.

### 4.2. Learning a compensation function

The compensation function $\dot{f}^{\text{proj}}_{\boldsymbol{\gamma}}(\alpha)$ modifies the shear reference displacements to counteract the parasitic effects in the $\alpha$-domain, as given by:

$$\dot{\tilde{r}}_{S_i}(\alpha) = \dot{r}_{S_i}(\alpha) + \dot{f}^{\text{proj}}_{\boldsymbol{\gamma}}(\alpha), \tag{35}$$

where $\dot{r}_{S_i}(\alpha)$ is the nominal reference defined in (18), and $\dot{f}^{\text{proj}}_{\boldsymbol{\gamma}}(\alpha)$ is a compensation function with parameters $\boldsymbol{\gamma}$. When these modified references $\dot{\tilde{r}}_{S_i}(\alpha)$ are used in control law (30) with $\hat{M}_e \approx M_e$, this results in $y_e \approx \tilde{r}_e$, i.e., the motion of the shears approximately equals the modified references. The goal of the compensation function is then to minimize the tracking error of the mover:

$$\varepsilon_j(t_k) := r(t_k) - y_j(t_k), \tag{36}$$

where $j$ is a trial number, and the reference is defined as

$$r(t_k) := \hat{G}(q)\dot{r}_{S_i}(t_k), \tag{37}$$

with $\hat{G}(q) \approx G(q)$ a model detailed in Section 4.4.1. The next sections detail how the compensation function $\dot{f}^{\text{proj}}_{\boldsymbol{\gamma}}(\alpha)$ is constructed from data over several trials to minimize $\|\varepsilon_j\|_2$, starting with the parametrization of $\dot{f}^{\text{proj}}_{\boldsymbol{\gamma}}(\alpha)$.

#### 4.2.1. Parametrization of the compensation function

The compensation function $\dot{f}^{\text{proj}}_{\boldsymbol{\gamma}}(\alpha)$ is parametrized as a piecewise-linear function to accommodate for the limited computational resources available on control hardware. First, define a grid of $n_\gamma$ points $\alpha_c \in [0, 2\pi)$, each equidistantly spaced $\Delta_\gamma$ apart. Next, define

$$\dot{f}^{\text{proj}}_{\boldsymbol{\gamma}}(\alpha) = \boldsymbol{\psi}^\top(\alpha)\boldsymbol{\gamma}, \tag{38}$$

where $\boldsymbol{\psi}(\alpha) \in \mathbb{R}^{n_\gamma}$ is a vector with only two nonzero elements, namely elements $c$ and $c+1$, the two elements on the grid that surround $\alpha$. These two elements of $\boldsymbol{\psi}(\alpha)$ are given by the linear interpolation

$$\psi_c(\alpha) = \frac{\alpha_{c+1} - \alpha}{\Delta_\gamma}, \quad \psi_{c+1}(\alpha) = \frac{\alpha - \alpha_c}{\Delta_\gamma}. \tag{39}$$

The next section describes how the model parameters are iteratively updated from data.

#### 4.2.2. Iteratively learning $\boldsymbol{\gamma}$ from data

The disturbance $\dot{d}(\alpha)$ is unknown, so the parameters $\boldsymbol{\gamma}$ cannot be determined directly. Instead, the repetitive nature of $\alpha$-domain disturbances is leveraged, updating $\boldsymbol{\gamma}$ iteratively using measurements of the mover position to reduce the tracking error.

First, at trial $j = 0$ with $\boldsymbol{\gamma}_0 = \mathbf{0}$ and zero initial conditions, an experiment is carried out with control law (30) and reference (35). Next, the system is reset to its initial state and the following update law is applied:

$$\dot{f}_{j+1}(t_k) = Q(q)(\dot{f}^{\text{proj}}_{\boldsymbol{\gamma}_j}(t_k) + L(q)\varepsilon_j(t_k)), \tag{40}$$

where $Q$ and $L$ are LTI filters detailed in Section 4.4.2. To facilitate the projection of this feedforward signal to the basis $\boldsymbol{\psi}(\alpha)$, a lifted notation is introduced. The model $\hat{G}(q)$ is represented in finite-time lifted notation by its impulse response matrix $\hat{\mathbf{G}}$. This matrix captures the input–output relationship over $N$ samples, assuming zero initial conditions, and is constructed from the impulse response coefficients $\hat{g}_k$ as:

$$\hat{\mathbf{G}} = \begin{bmatrix} \hat{g}_0 & 0 & \cdots & 0 \\ \hat{g}_1 & \hat{g}_0 & \cdots & 0 \\ \hat{g}_2 & \hat{g}_1 & \cdots & 0 \\ \vdots & \vdots & \ddots & \vdots \\ \hat{g}_{N-1} & \hat{g}_{N-2} & \cdots & \hat{g}_0 \end{bmatrix}. \tag{41}$$

This structure generalizes to any linear time-invariant (LTI) system but is here used specifically for $\hat{G}(q)$. Using this notation, the time-domain signal $\dot{f}_{\boldsymbol{\gamma}_{j+1}}(t_k)$ obtained from (40) is projected to the low-order basis (38) by minimizing

$$\tilde{J}_{\boldsymbol{\gamma}_{j+1}} = \|\hat{\mathbf{G}}(\dot{\mathbf{f}}_{j+1} - \dot{\mathbf{f}}^{\text{proj}}_{\boldsymbol{\gamma}_{j+1}})\|_2^2, \tag{42}$$

where $\dot{\mathbf{f}}_{j+1} \in \mathbb{R}^N$ stacks $\dot{f}_{j+1}(t_k)$ for all samples $t_k$, $k \in \{1, \dots, N\}$ and the premultiplication with $\hat{\mathbf{G}}$ reflects the desire to match the projected error to the predicted error rather than the compensation signal itself. The solution to (42) is then given by:

$$\boldsymbol{\gamma}_{j+1} = (\boldsymbol{\Psi}^\top\hat{\mathbf{G}}^\top\hat{\mathbf{G}}\boldsymbol{\Psi})^{-1}\boldsymbol{\Psi}^\top\hat{\mathbf{G}}^\top\hat{\mathbf{G}}\dot{\mathbf{f}}_{j+1}, \tag{43}$$

with $\boldsymbol{\Psi} = [\boldsymbol{\psi}(\alpha(t_1)), \dots, \boldsymbol{\psi}(\alpha(t_N))]^\top$.

Update law (40) and projection (43) are the two main components to compensating for $\alpha$-domain disturbances, shown in Algorithm 2. The next section proves that Algorithm 2 leads to monotonic convergence of the compensation signal.

### 4.3. Convergence

The following lemma states the conditions under which the compensation signal converges monotonically.

**Lemma 4.1.** *Using update law (40) with $L(q)$ and $Q(q)$ causal and stable, followed by projection (43), the compensation signal $\dot{f}^{\text{proj}}_{\boldsymbol{\gamma}_j}(\alpha(t_k))$ is monotonically convergent in the two-norm as $j \to \infty$ if and only if*

$$\overline{\sigma}\left(\boldsymbol{\Psi}(\boldsymbol{\Psi}^\top\hat{\mathbf{G}}^\top\hat{\mathbf{G}}\boldsymbol{\Psi})^{-1}\boldsymbol{\Psi}^\top\hat{\mathbf{G}}^\top\hat{\mathbf{G}}\mathbf{Q}(\mathbf{I} - \mathbf{L}\mathbf{G})\right) < 1, \tag{44}$$

*where $\overline{\sigma}$ denotes the maximum singular value and $\mathbf{G}$, $\mathbf{Q}$, and $\mathbf{L}$ are the impulse response matrices of $G(q)$, $Q(q)$, and $L(q)$, respectively, in the form of (41).*

**Proof** ([33]). See Appendix A. ■

This convergence condition hinges upon the design of $L(q)$ and $Q(q)$. The following theorem provides a frequency-domain convergence condition that facilitates the design of these filters later. Note that neither Lemma 4.1 nor Theorem 1 rely on the drive frequency $f_\alpha$ used for data collection to prove convergence.

**Algorithm 3** Unified framework: flexible feedforward control of piezo-stepper actuators

**Require:** Initial waveforms Eq. (18), constant hysteresis models Eq. (7), range $\mathcal{F}$ of application-relevant drive frequencies Eq. (17).

1: Perform Algorithm 1 to collect datasets $\mathcal{D}_e$.
2: Obtain hysteresis models $\hat{M}_{\theta_{e^i}}$ from Eq. (27).
3: Solve Eq. (33) for each $f_\alpha \in \mathcal{F}$ to obtain $g^{\text{LUT}}_{e,\max}(f_\alpha)$ and $g^{\text{LUT}}_{e,\min}(f_\alpha)$ in Eq. (34).
4: Obtain a model $\hat{G} \approx G$ using Eq. (47).
5: Perform Algorithm 2 in both directions to obtain modified shear references $\dot{\tilde{r}}_{S_i}(\alpha)$ in Eq. (49).
6: **return** Control law Eq. (30) with models $\hat{M}_{\theta_{e^i}}$ and modified shear references $\dot{\tilde{r}}_{S_i}(\alpha)$, with Eq. (18) and Eq. (34).

**Theorem 1.** *Using update law (40) with $L(q)$ and $Q(q)$ causal and stable, followed by projection (43), the compensation signal $f^{\text{proj}}_{\gamma_j}(\alpha(t_k))$ is monotonically convergent in the two-norm as $j \to \infty$ if*

$$\sup_{\omega\in[0,\pi]} |Q(e^{j\omega})(1 - L(e^{j\omega})G(e^{j\omega}))| < 1. \tag{45}$$

**Proof** (*[33]*). See Appendix B. ■

In contrast to [33], which addresses convergence of compensation functions for single-input single-output (SISO) systems in a closed loop setting, Lemma 4.1 and Theorem 1 apply to the open-loop feedforward scheme depicted in Fig. 5, where the two shear references are simultaneously updated by a single compensation function through (35).

The next section provides some guidelines for designing filters $L(q)$ and $Q(q)$ that satisfy Theorem 1, among other implementation aspects. Moreover, Algorithm 3 summarizes the unified framework of feedforward control for piezo-stepper actuators, combining the compensation of $\alpha$-domain disturbances with rate-dependent hysteresis compensation.

### 4.4. Implementation aspects

This section discusses practical considerations for the implementation of Algorithm 2, starting with obtaining $\hat{G}(q)$.

#### 4.4.1. Identification of $\hat{G}(q) \approx G(q)$

To obtain a model $\hat{G}(q) \approx G(q)$, which is a prerequisite for Algorithm 2, the first step is to measure a frequency response function $G(e^{j\omega}) := y(e^{j\omega})/y_{\text{true}}(e^{j\omega})$. This cannot be done directly as $y_{\text{true}}$ is unknown. Instead, an indirect approach is taken, where $G_{S_1}$ and $G_{S_2}$ are measured, defined as

$$G_{S_i}(e^{j\omega}) := \frac{y(e^{j\omega})}{u_{S_i}(e^{j\omega})}. \tag{46}$$

These systems are measured using standard open-loop system identification, where $u_{S_i}$ is excited by a random-phase multisine signal while in contact with the mover, and the mover position $y$ is recorded, in a separate experiment per shear. The data is averaged out over multiple realizations of the random-phase multisines to obtain Best Linear Approximations (BLAs) $\hat{G}_{S_1,\text{BLA}}(e^{j\omega})$ and $G_{S_2,\text{BLA}}(e^{j\omega})$, see [34] for details. The frequency response function of the sensor is then approximated as the scaled average

$$\hat{G}(e^{j\omega}) = \frac{T_s}{e^{j\omega} - 1} \cdot \frac{1}{2c_G} \left( \hat{G}_{S_1,\text{BLA}}(e^{j\omega}) + \hat{G}_{S_2,\text{BLA}}(e^{j\omega}) \right), \tag{47}$$

where the first term represents a discrete-time integrator and $c_G$ is a scaling factor defined as

$$c_G = \frac{1}{2} \left( \hat{G}_{S_1,\text{BLA}}(e^{j\omega_0}) + \hat{G}_{S_2,\text{BLA}}(e^{j\omega_0}) \right), \tag{48}$$

with $\omega_0$ the lowest measured frequency. This approximation assumes that the sensor $G(q)$ behaves as a discrete-time integrator at low frequencies. Section 5.4 discusses the limitations of this approximation. Finally, a low-order parametric fit $\hat{G}(q)$ is made of $\hat{G}(e^{j\omega})$.

#### 4.4.2. Design of $L(q)$ and $Q(q)$

The learning filter $L(q)$ and the robustness filter $Q(q)$ must satisfy condition (45) and be causal and stable. First, define $L(q) = \beta q^{-d}\hat{G}^{-1}(q)$, where $\beta \in (0, 1]$ is a learning gain and $d$ is the relative degree of $\hat{G}(q)$. Lower values of $\beta$ lead to better mitigation of trial-varying disturbances at the cost of slower convergence, see [35]. Secondly, design $Q(q)$ such that condition (45) holds, e.g., by parametrizing $Q(q)$ as a lowpass filter.

#### 4.4.3. Direction-dependent compensation functions

Mechanical misalignments lead to a disturbance that is repeatable in the $\alpha$-domain, but is dependent on the direction of motion. Indeed, when the clamps push the shears onto the mover at an angle, this results in a different force depending on whether the shear is expanding or contracting. Therefore, Algorithm 2 is performed twice: once using a positive drive frequency $f_\alpha$ and once using $-f_\alpha$. This results in two compensation functions, $f^{\text{proj}}_{\gamma,+}$ and $f^{\text{proj}}_{\gamma,-}$. The reference for control law (30) then becomes

$$\dot{\tilde{r}}_{S_i}(\alpha) = \begin{cases} \dot{r}_{S_i}(\alpha) + f^{\text{proj}}_{\gamma,+}(\alpha) & \text{if } f_\alpha \geq 0, \\ \dot{r}_{S_i}(\alpha) + f^{\text{proj}}_{\gamma,-}(\alpha) & \text{if } f_\alpha < 0. \end{cases} \tag{49}$$

## 5. Experimental results

This section shows experimentally that the developed approach achieves high positioning performance for piezo-stepper actuators despite hysteresis and mechanical misalignments. The experimental setup is described in Section 2.1.

First, the implementation of the hysteresis compensation method of Section 3 is explained, before the compensation of mechanical misalignments of Section 4 is addressed.

### 5.1. Hysteresis compensation

Following the procedure in Section 3, hysteresis models $\hat{M}_{e,\text{LUT}}$ are created using measurements of the currents. A total of $F = 52$ drive frequencies between 0.3 and 100 Hz are chosen. This choice for $F$ is based on empirical assessment of the smoothness of the resulting hysteresis data in the $|\dot{u}_e|$-direction, see Fig. 6. This figure displays the measured data and the fitted model $\hat{M}_{S_1,\text{LUT}}$ for shear $S_1$, demonstrating a very good match between the data and the model for all measured voltage rates and absements. For comparison, the rate-independent Ramberg–Osgood model presented in [13] is also shown, drawn in red for several voltage rates. This alternative model is given by

$$\hat{M}_{S_1,\text{RO}}(u_{S_1,a}, \mathbf{h}) = h_1 + h_2 u^{h_3}_{S_1,a}, \tag{50}$$

with parameters $\mathbf{h} = [h_1, h_2, h_3]^\top$ given by the unique solution to the separable least-squares problem

$$\mathbf{h} = \arg\min_{\mathbf{h}} \sum_{i=1}^{n} \left( \hat{M}_{S_1,\text{RO}}(u_{S_1,a,i}, \mathbf{h}) - m_{S_1,i} \right)^2, \tag{51}$$

see [13] for details. Since the Ramberg–Osgood model is rate-independent, it does not accurately reflect the hysteresis behavior at low or high voltage rates, whereas the rate-dependent model presented in this paper does, as clearly seen in Fig. 6. To be precise, the root-mean-square (RMS) error between the developed hysteresis model and the data is $0.022\,\text{A s V}^{-1}$, while the Ramberg–Osgood model has an RMS prediction error of $0.076\,\text{A s V}^{-1}$. This is a considerable difference, relative to the mean of the observations, which is $0.75\,\text{A s V}^{-1}$.

The hysteresis measurements of the first clamp and the first shear are displayed in Fig. 7, which shows a clear direction-dependency in the

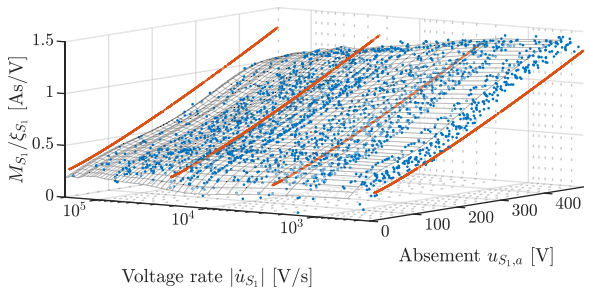


**Fig. 6.** Measurements of the hysteresis function for the first shear (•), with the fitted rate-dependent model $\hat{M}_{S_1,\mathrm{LUT}}$ (□). A rate-independent Ramberg–Osgood model [13] (—), fitted on all data and plotted along four voltage rates, does not accurately reflect the measurements at high or low voltage rates, whereas the developed rate-dependent model matches the recorded data quite well. The data, sub-sampled for visibility, results from a single experiment described by Algorithm 1 with $F = 52$ different drive frequencies between 0.3 Hz and 100 Hz in either direction.

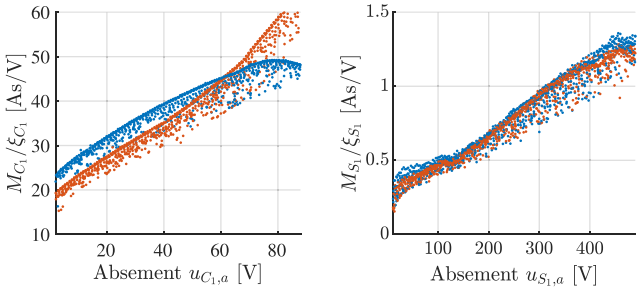


(a) Clamp $C_1$ (b) Shear $S_1$

**Fig. 7.** Hysteresis measurements of forwards (•) and backwards (•) motions for all measured voltage rates together. (a) The first clamp shows much more significant direction-dependency than (b) the first shear. Note that (b) is a side-view of the data in Fig. 6.

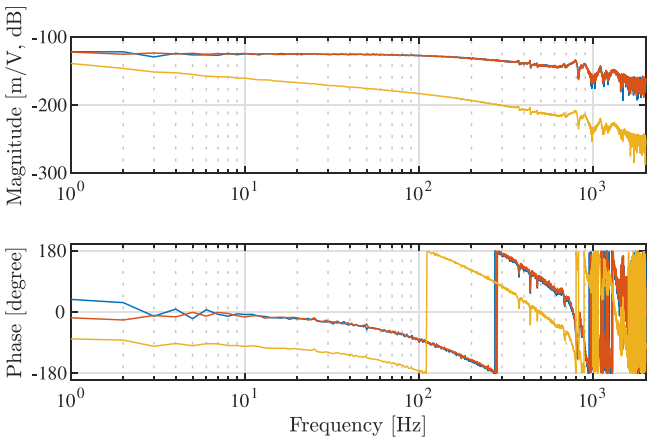


**Fig. 8.** Bode plots of the shear BLAs $\hat{G}_{S_1,\mathrm{BLA}}(e^{j\omega})$ (—) and $\hat{G}_{S_2,\mathrm{BLA}}(e^{j\omega})$ (—), used to approximate the scaled sensor dynamics $c_G\hat{G}(e^{j\omega})$ (—).

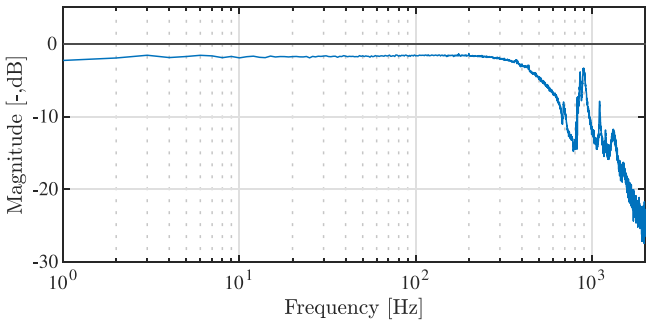


**Fig. 9.** Magnitude plot of $Q(e^{j\omega})(1 - L(e^{j\omega})\hat{G}(e^{j\omega}))$. The condition for convergence of ILC in Theorem 1 holds since this magnitude is below 0 dB for all frequencies.

clamp. Similar direction-dependent hysteresis behavior is seen in the second clamp, but only to a limited extent in either of the shears. The direction-dependency is accounted for by separately modeling $\hat{M}_{\theta_{e^+}}$ and $\hat{M}_{\theta_{e^-}}$, see (16) and (19).

Finally, these models are used to create lookup tables (34) as explained in Section 3.3.2 to mitigate integrator drift. From these tables, it follows that the reference stroke required to reach the voltage bounds gradually decreases from 3.8 µm to 3 µm between drive frequencies of 1 and 100 Hz. With these elements in place, control law (30) allows compensation of hysteresis in the piezo-stepper actuator.

### 5.2. Compensation of $\alpha$-dependent disturbances

With hysteresis compensated through control law (30), the next step is compensating $\alpha$-dependent disturbances. First, the LTI model $\hat{G}(q)$ is identified as described in Section 4.4.1, see Fig. 8. Subsequently, $L(q)$ and $Q(q)$ are designed as described in Section 4.4.2, with $\beta = 0.2$ and $Q(q)$ a 2nd order lowpass filter with 500 Hz cutoff frequency.

Finally, Algorithm 2 is followed with drive frequency $f_\alpha = 2$ Hz. This drive frequency is chosen arbitrarily; other drive frequencies up to 50 Hz have also been tested and yield similar results to those presented here. The convergence condition from Theorem 1 is visualized in Fig. 9, showing that the designed $Q$ and $L$ filter together lead to a convergent ILC scheme. The next section presents the results.

### 5.3. Results

This section compares the performance of three different feedforward control strategies:

S1: Traditional feedforward control: control law (30) with reference displacements $\rho_e(\alpha, f_\alpha)$ and constant hysteresis models $\hat{M}_e = c_{M,e}$.

S2: Rate-dependent hysteresis compensation: control law (30) with reference displacements $\rho_e(\alpha, f_\alpha)$ and rate-dependent hysteresis models (19).

S3: Rate-dependent hysteresis compensation in conjunction with $\alpha$-domain disturbance compensation: control law (30) with clamp reference displacements $\rho_{C_i}(\alpha, f_\alpha)$, and modified shear reference displacements $\dot{\tilde{r}}_{S_i}$ from Algorithm 2, and rate-dependent hysteresis models (19).

The performance of traditional strategy S1 is shown in Fig. 3 and discussed in Section 2.4. The following section presents the results of strategies S2 and S3 for a single drive frequency $f_\alpha = 2$ Hz, after which all three strategies are compared for a range of drive frequencies.

#### 5.3.1. Performance at $f_\alpha = 2$ Hz

Fig. 10 shows the reduction in root-mean-square deviation (RMSD) of the tracking error over twenty iterations of Algorithm 2, showing a reduction from 40 nm to 8.7 nm over the iterations. The first and last iterations correspond to control strategies S2 and S3, respectively. Fig. 11 compares their tracking errors, confirming that the learned compensation function effectively eliminates the disturbance.

The remaining error is dominated by an oscillation around 3250 Hz, as seen in the reverse cumulative amplitude spectrum in Fig. 12, likely due to flexible dynamics. Since this oscillation does not repeat in the $\alpha$-domain, it remains uncorrected by ILC, contributing approximately

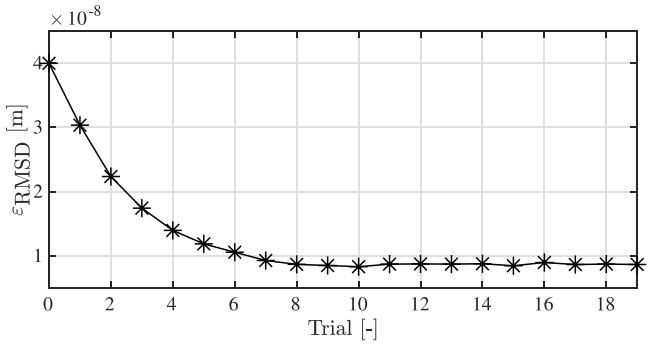


**Fig. 10.** Convergence of the root-mean-square deviation of the tracking error during Algorithm 2, over the course of twenty trials. Note that hysteresis compensation is active in all trials through control law (30).

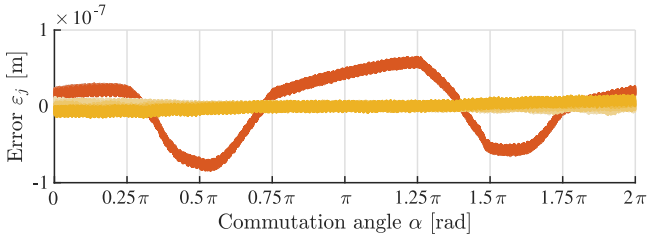


**Fig. 11.** Experimentally measured tracking error of the first (—, S2) and twentieth (—, S3) iteration of Algorithm 2, with hysteresis compensation active in both experiments. The six forwards steps are displayed separately, each with different color saturation and their mean set to zero.

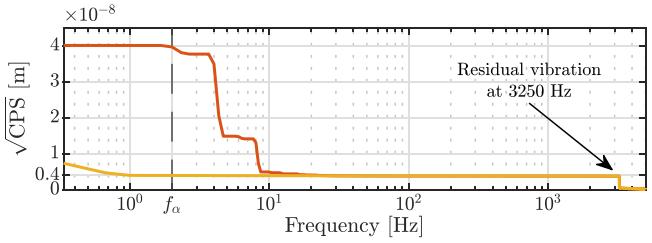


**Fig. 12.** Reverse cumulative amplitude spectrum of the tracking error $\varepsilon$ in the first (—) and last (—) iteration of Algorithm 2 at $f_\alpha = 2$ Hz. As most of the remaining error appears below the drive frequency (- -), which exceeds the $\alpha$-domain, or at very high frequencies, the $\alpha$-domain disturbances are considered eliminated.

3.5 nm to the RMSD error. Additionally, frequencies below $f_\alpha$ exceed the $\alpha$-domain and are not addressed by the compensation. The next section shows that these performance improvements generalize to other drive frequencies as well.

### 5.3.2. *Performance across different drive frequencies*

To assess the flexibility of the approach, the performance is compared for drive frequencies ranging from 0.4 to 100 Hz, see Fig. 13. When using traditional feedforward strategy S1, the error remains high across all frequencies, see also Fig. 3. Although rate-dependent hysteresis compensation (S2) improves the performance according to Fig. 13, it does not address the $\alpha$-dependent disturbances. Utilizing the compensation function $f'^{\text{proj}}(\alpha)$ obtained from Algorithm 2 (S3) yields a significant improvement for all drive frequencies: a fifteenfold improvement at $f_\alpha = 2$ Hz, when compared to S1. These conclusions

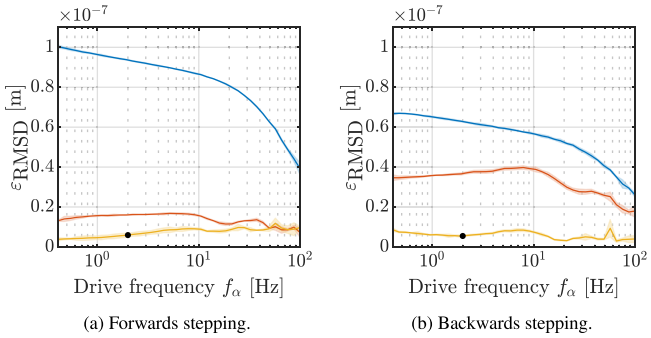


**Fig. 13.** Root-mean-square deviation of the position error, averaged over three subsequent steps, for different drive frequencies. Traditional feedforward control (—, S1) leads to consistently large error. Hysteresis compensation (—, S2) by itself results in a performance increase, but more importantly, it is a prerequisite for Algorithm 2 (—, S3), which reduces the error for all drive frequencies after converging solely with $f_\alpha = 2$ Hz (•). Shaded areas reflect two standard deviations.

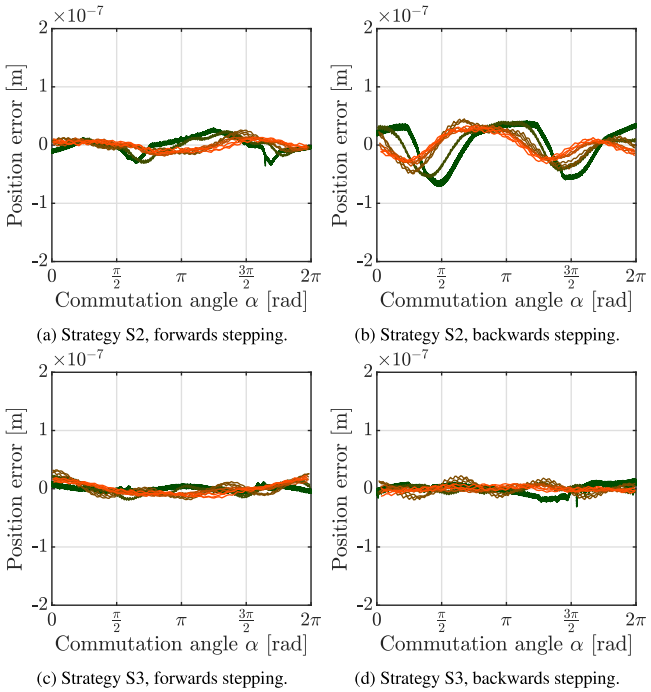


**Fig. 14.** Position error of the mover against the commutation angle $\alpha$, after hysteresis compensation (S2, top) and after hysteresis compensation in conjunction with compensation of mechanical misalignments (S3, bottom). The data reflects a range of constant drive frequencies between 0.4 Hz (—) and 100 Hz (—), showing three steps per frequency. These plots complement the results of the uncompensated situation S1 in Fig. 3, showing that the developed approach effectively reduces the tracking error for all drive frequencies.

are supported by Fig. 14, showing the same data in the $\alpha$-domain for a smaller range of drive frequencies.

Moreover, an interesting difference between forwards and backwards stepping is observed in Fig. 13. With traditional feedforward, the performance is better in the backwards direction, but when only hysteresis is compensated, the performance is better in the forwards direction. This suggests that the effect of $\alpha$-dependent disturbances is higher in the backwards direction, but that hysteresis is less pronounced in this direction. The compensation of $\alpha$-dependent disturbances in conjunction with hysteresis compensation (S3) leads to a similar performance

in both directions, showing that the developed approach effectively removes both direction-dependency and rate-dependency in the system.

### 5.4. Discussion

This section addresses several further observations drawn from the experimental results, as well as limitations and further opportunities.

#### 5.4.1. Limitations of the capacitive position sensor

The capacitive sensor $G(q)$ has a cutoff frequency of approximately 100 Hz, significantly impacting the phase and magnitude of the measured mover position at higher drive frequencies. This sensor is used in Algorithm 2 and to assess performance. In Algorithm 2, the measured mover position is filtered with $L \approx G^{-1}$ before projecting the compensation signal to the $\alpha$-domain, essentially correcting for these sensor dynamics.

However, the sensor dynamics are not corrected for in the performance assessment, leading to a discrepancy between the measured and actual performance. The result is that Figs. 3 and 14 display more variation over frequencies than what can be explained by hysteresis only. Similarly, Fig. 13 shows a reduced RMSD error for high drive frequencies when using traditional feedforward. This is explained by the sensor dynamics as well, since lowpass effects in the sensor reduce the measured error ripples at high drive frequencies.

#### 5.4.2. Artifacts in the identified sensor model

The identified sensor model in Fig. 8 suggests the presence of flexible dynamics at high frequencies. These dynamics do not reflect the sensor itself but are rather an artifact from the approximation (47). By constructing $\hat{G}(q)$ from the BLAs of the shears where voltage is the input, flexible dynamics of the piezo element may end up in $\hat{G}(q)$. This does not pose a problem for the approach: as long as the magnitude of $1 - Q(e^{j\omega})(1 - L(e^{j\omega})G(e^{j\omega}))$ in Fig. 9 remains robustly below 0 dB, the ILC scheme converges.

#### 5.4.3. Systematic effects in the hysteresis model

Finally, the identified hysteresis models $\hat{M}_e(\dot{u}_e, u_{e,a})$ are obtained from measurements where the hysteresis of the piezo elements is unavoidably coupled with systematic contributions from contact dynamics and linear dynamics. Such systematic effects, impacting the piezo displacements while being dependent on voltage rate or absement, end up in $\hat{M}_e(\dot{u}_e, u_{e,a})$ and are also compensated for by the inversion in control law (30). This improves performance, and any residual, unmodeled $\alpha$-dependent effects are subsequently targeted by Algorithm 2. Therefore, although $\hat{M}_e$ captures more than just hysteresis, the total framework robustly compensates for all these effects, ensuring accurate positioning for arbitrary drive frequencies.

#### 5.4.4. Industrial applicability

While the developed approach is demonstrated on a specific piezo-stepper actuator, see Fig. 4, it is broadly applicable. The main hardware requirements for Algorithm 3 are threefold. First, a piezo-stepper actuator with a voltage amplifier is required.

Second, a real-time control platform with sufficient memory and computational power is needed. The lookup tables for hysteresis, reference strokes and compensation of $\alpha$-domain disturbances, as configured in the experiments presented in this section, require approximately 52 kB of storage when using single-precision floating-point numbers. This size may be reduced at marginal performance costs by increasing the coarseness of the lookup tables; no such optimizations have been done in this paper. Moreover, the implementation of control law (30), including reference generation and linear interpolation of the lookup tables, requires a total of approximately 140 floating-point operations (FLOP), leading to $1.4{\cdot}10^6$ FLOP/s at $F_s = 10^4$ Hz.

Third, sensors for offline measurement of piezo currents and mover position are needed only during calibration or recalibration. After calibration with Algorithm 3, the feedforward control law operates without sensors, hence avoiding the use of additional hardware with associated maintenance costs. If hysteresis or misalignments change over time, recalibration is possible by reinstalling the sensors and repeating Algorithm 3.

## 6. Conclusion

The developed control framework for piezo-stepper actuators achieves accurate and flexible positioning by compensating hysteresis and misalignments. The framework is validated on one specific type of piezo-stepper actuator. It is directly applicable to other piezo and piezo-stepper designs that suffer from hysteresis or mechanical misalignments. First, a rate-dependent hysteresis function is modeled from data and used in a feedforward control law that decouples the piezo input signals from their history. Next, iterative learning control (ILC) is applied to learn a compensation function added to the shear waveforms, ensuring a constant mover velocity even when the piezo elements are imperfectly aligned.

The approach relies on lookup tables and a low number of arithmetic operations during real-time evaluation, facilitating implementation on embedded control platforms. Moreover, as this is a feedforward approach, its improvements in positioning accuracy enable the reduction of the feedback gain in closed loop piezo-stepper control, reducing the amplification of measurement noise. In some cases, this may allow for cost savings on high-precision position sensors or even eliminate the need for a position sensor entirely.

Finally, experimental results confirm that the improvement in positioning accuracy is robust to changes in the reference velocities, further increasing the industrial applicability of the method. These results show that the developed feedforward approach achieves accurate positioning of piezo-stepper actuators, enabling their use in applications that require high precision, stiffness, and task flexibility, without expensive position sensors.

## CRediT authorship contribution statement

**Max van Meer:** Writing – review & editing, Writing – original draft, Visualization, Validation, Methodology, Formal analysis, Conceptualization. **Tim van Meijel:** Visualization, Validation, Software, Methodology, Investigation, Formal analysis, Conceptualization. **Emile van Halsema:** Writing – review & editing, Supervision, Resources. **Edwin Verschueren:** Writing – review & editing, Resources. **Gert Witvoet:** Writing – review & editing, Supervision. **Tom Oomen:** Writing – review & editing, Supervision.

## Declaration of competing interest

The authors declare that they have no known competing financial interests or personal relationships that could have appeared to influence the work reported in this paper.

## Appendix A. Proof of Lemma 4.1

First, the projection (43) is substituted in $\dot{\mathbf{f}}^{\text{proj}}_{\boldsymbol{\gamma}_{j+1}} = \boldsymbol{\Psi}\boldsymbol{\gamma}_{j+1}$ to obtain

$$\dot{\mathbf{f}}^{\text{proj}}_{\boldsymbol{\gamma}_{j+1}} = \boldsymbol{\Psi}(\boldsymbol{\Psi}^\top \hat{\mathbf{G}}^\top \hat{\mathbf{G}} \boldsymbol{\Psi})^{-1} \boldsymbol{\Psi}^\top \hat{\mathbf{G}}^\top \hat{\mathbf{G}} \dot{\mathbf{f}}_{j+1}. \tag{A.1}$$

With update law (40), this becomes

$$\dot{\mathbf{f}}^{\text{proj}}_{\boldsymbol{\gamma}_{j+1}} = \boldsymbol{\Psi}(\boldsymbol{\Psi}^\top \hat{\mathbf{G}}^\top \hat{\mathbf{G}} \boldsymbol{\Psi})^{-1} \boldsymbol{\Psi}^\top \hat{\mathbf{G}}^\top \hat{\mathbf{G}} \mathbf{Q} (\dot{\mathbf{f}}^{\text{proj}}_j + \mathbf{L}\boldsymbol{\varepsilon}_j). \tag{A.2}$$

Next, express the error (36) as

$$\boldsymbol{\varepsilon}_j = (\hat{\mathbf{G}} - \mathbf{G})\dot{\mathbf{r}}_{S_i} - \mathbf{G}\dot{\mathbf{f}}^{\text{proj}}_{\boldsymbol{\gamma}_j} - \mathbf{d}_j, \tag{A.3}$$

and substitute it into (A.2) to obtain

$$\begin{aligned}\dot{\mathbf{f}}^{\text{proj}}_{\gamma_{j+1}} =& \boldsymbol{\Psi}(\boldsymbol{\Psi}^\top\hat{\mathbf{G}}^\top\hat{\mathbf{G}}\boldsymbol{\Psi})^{-1}\boldsymbol{\Psi}^\top\hat{\mathbf{G}}^\top\hat{\mathbf{G}}\mathbf{Q} \\ &\cdot\left((\mathbf{I}-\mathbf{LG})\dot{\mathbf{f}}^{\text{proj}}_j + \mathbf{L}\left((\hat{\mathbf{G}}-\mathbf{G})\dot{\mathbf{r}}_{S_i}-\mathbf{d}_j\right)\right).\end{aligned} \tag{A.4}$$

Define the matrix

$$\mathbf{A} = \mathbf{DQ}(\mathbf{I}-\mathbf{LG}), \tag{A.5}$$

and the vector

$$\mathbf{b}_j = \mathbf{DQL}\left((\hat{\mathbf{G}}-\mathbf{G})\dot{\mathbf{r}}_{S_i}-\mathbf{d}_j\right), \tag{A.6}$$

where

$$\mathbf{D} := \boldsymbol{\Psi}\left(\boldsymbol{\Psi}^\top\hat{\mathbf{G}}^\top\hat{\mathbf{G}}\boldsymbol{\Psi}\right)^{-1}\boldsymbol{\Psi}^\top\hat{\mathbf{G}}^\top\hat{\mathbf{G}}. \tag{A.7}$$

Then, the update equation (A.4) simplifies to

$$\dot{\mathbf{f}}^{\text{proj}}_{\gamma_{j+1}} = \mathbf{A}\dot{\mathbf{f}}^{\text{proj}}_j + \mathbf{b}_j. \tag{A.8}$$

Since $\dot{\mathbf{r}}_{S_i}$, $\mathbf{d}_j$, and $(\hat{\mathbf{G}}-\mathbf{G})$ are bounded, the vector $\mathbf{b}_j$ is bounded. Moreover, when $\overline{\sigma}(\mathbf{A}) < 1$, it follows that $\|\mathbf{A}^j\|_2 \to 0$ as $j \to \infty$. By iterating the update equation, this becomes

$$\dot{\mathbf{f}}^{\text{proj}}_j = \mathbf{A}^j\dot{\mathbf{f}}^{\text{proj}}_0 + \sum_{k=0}^{j-1}\mathbf{A}^{j-1-k}\mathbf{b}_k. \tag{A.9}$$

The term $\mathbf{A}^j\dot{\mathbf{f}}^{\text{proj}}_0$ tends to zero because $\|\mathbf{A}^j\|_2 \to 0$. Since $\mathbf{b}_k$ is bounded and $\|\mathbf{A}^{j-1-k}\|_2$ decreases with each iteration, the summation converges to a finite limit. Therefore, when the condition in (44) holds, the sequence $\|\dot{\mathbf{f}}^{\text{proj}}_j\|_2$ decreases monotonically and converges in the two-norm as $j \to \infty$. ■

## Appendix B. Proof of Theorem 1

The condition (44) of Lemma 4.1 is bounded by

$$\overline{\sigma}(\mathbf{DQ}(\mathbf{I}-\mathbf{LG})) \le \overline{\sigma}(\mathbf{D})\overline{\sigma}(\mathbf{Q}(\mathbf{I}-\mathbf{LG})), \tag{B.1}$$

with $\mathbf{D}$ defined in (A.7). Hence, condition (44) is satisfied if $\overline{\sigma}(\mathbf{D})\overline{\sigma}(\mathbf{Q}(\mathbf{I}-\mathbf{LG})) \le 1$. This is the case if (45) holds and $\overline{\sigma}(\mathbf{D}) = 1$. To see that $\overline{\sigma}(\mathbf{D}) = 1$, note that $\mathbf{D}$ is idempotent, i.e., $\mathbf{D}^2 = \mathbf{D}$. Since all eigenvalues $\lambda_i$ of an idempotent matrix are either 0 or 1, and $\mathbf{D}$ is not a zero matrix, $\mathbf{D}$ has a largest eigenvalue $\overline{\lambda} = 1$, and hence, $\overline{\sigma}(\mathbf{D}) = 1$. As such, condition (44) reduces to

$$\overline{\sigma}(\mathbf{Q}(\mathbf{I}-\mathbf{LG})) \le 1. \tag{B.2}$$

Finally, it follows directly from [36, Theorem 8] that when $L(q)$ and $Q(q)$ are stable and causal, it holds that

$$\sup_{\omega\in[0,\pi]}|Q(e^{j\omega})(1-L(e^{j\omega})G(e^{j\omega}))| < 1 \implies \overline{\sigma}(\mathbf{Q}(\mathbf{I}-\mathbf{LG})) \le 1. \tag{B.3}$$

Hence, (45) is a sufficient condition for convergence. ■

## Data availability

Data will be made available on request.

## References


[1] Fleming AJ, Leang KK. Design, modeling and control of nanopositioning systems. Advances in industrial control, Cham: Springer International Publishing; 2014, http://dx.doi.org/10.1007/978-3-319-06617-2.

[2] Li J, Huang H, Morita T. Stepping piezoelectric actuators with large working stroke for nano-positioning systems: A review. Sens. Actuators, A: Phys 2019;292:39–51. http://dx.doi.org/10.1016/j.sna.2019.04.006.

[3] Kanchan M, Santhya M, Bhat R, Naik N. Application of modeling and control approaches of piezoelectric actuators: A review. Technologies 2023;11(6). http://dx.doi.org/10.3390/technologies11060155.

[4] Den Heijer M, Fokkema V, Saedi A, Schakel P, Rost MJ. Improving the accuracy of walking piezo motors. Rev Sci Instrum 2014;85(5). http://dx.doi.org/10.1063/1.4878624.

[5] Mohith S, Upadhya AR, Navin KP, Kulkarni SM, Rao M. Recent trends in piezoelectric actuators for precision motion and their applications: a review. Smart Mater Struct 2021;30(1). http://dx.doi.org/10.1088/1361-665X/abc6b9.

[6] Strijbosch N, Verschueren E, Tiels K, Oomen T. Control- motion feedforward tuning for hysteretic piezo actuators. Mikroniek 2021;4(2021):26–31.

[7] Ruan Z, Li Q, Guo L, Ding C. Feedback switching control of a walking piezoelectric actuator for trajectory tracking. Smart Mater Struct 2024;33(12). http://dx.doi.org/10.1088/1361-665X/ad912a.

[8] Merry RJE, Maassen MGJM, van de Molengraft MJG, van de Wouw N, Steinbuch M. Modeling and waveform optimization of a nano-motion piezo stage. IEEE/ASME Trans Mechatronics 2011;16(4):615–26. http://dx.doi.org/10.1109/TMECH.2010.2050209.

[9] Li RJ, Han ZZ. Survey of iterative learning control. Kongzhi Yu Juece/Control Decis 2005;20(9):961–6. http://dx.doi.org/10.1109/mcs.2006.1636313.

[10] Aarnoudse L, Strijbosch N, Tacx P, Verschueren E, Oomen T. Compensating commutation-angle domain disturbances with application to waveform optimization for piezo stepper actuators. Mechatronics 2023;94(15698). http://dx.doi.org/10.1016/j.mechatronics.2023.103016.

[11] Strijbosch N, Tacx P, Verschueren E, Oomen T. Commutation angle iterative learning control: Enhancing piezo-stepper actuator waveforms. IFAC-PapersOnLine 2019;52(15):579–84. http://dx.doi.org/10.1016/j.ifacol.2019.11.738.

[12] Franklin G, Powell JD, Emami-Naeini A. Feedback control of dynamic systems. Seventh ed.. New York; 1994.

[13] Strijbosch N, Tiels K, Oomen T. Memory-element-based hysteresis: Identification and compensation of a piezoelectric actuator. IEEE Trans Control Syst Technol 2023;31(6):2863–70. http://dx.doi.org/10.1109/TCST.2022.3214053.

[14] Ge P, Jouaneh M. Modeling hysteresis in piezoceramic actuators. Precis Eng 1995;17(3):211–21. http://dx.doi.org/10.1016/0141-6359(95)00002-U.

[15] Li Z, Zhang X, Su C-Y, Chai T. Nonlinear control of systems preceded by preisach hysteresis description: A prescribed adaptive control approach. IEEE Trans Control Syst Technol 2015;24(2):451–60. http://dx.doi.org/10.1109/TCST.2015.2441001.

[16] Kuhnen K. Modeling, identification and compensation of complex hysteretic nonlinearities: A modified prandtl-ishlinskii approach. Eur J Control 2003;9(4):407–18. http://dx.doi.org/10.3166/ejc.9.407-418.

[17] Chen J, Peng G, Hu H, Ning J. Dynamic hysteresis model and control methodology for force output using piezoelectric actuator driving. IEEE Access 2020;8:205136–47. http://dx.doi.org/10.1109/ACCESS.2020.3037216.

[18] Janaideh MA, Rakheja S, Su CY. Experimental characterization and modeling of rate-dependent hysteresis of a piezoceramic actuator. Mechatronics 2009;19(5):656–70. http://dx.doi.org/10.1016/j.mechatronics.2009.02.008.

[19] Hassani V, Tjahjowidodo T, Do TN. A survey on hysteresis modeling, identification and control. Mech Syst Signal Process 2014;49(1–2):209–33. http://dx.doi.org/10.1016/j.ymssp.2014.04.012.

[20] Cai J, Dong W, Nagamune R. A survey of Bouc-Wen hysteretic models applied to piezo-actuated mechanical systems: Modeling, identification, and control. J Intell Mater Syst Struct 2023;34(16):1843–63. http://dx.doi.org/10.1177/1045389X231157361.

[21] Chowdhury D, Al-Nadawi YK, Tan X. Dynamic inversion-based hysteresis compensation using extended high-gain observer. Automatica 2022;135:109977. http://dx.doi.org/10.1016/j.automatica.2021.109977.

[22] Yang M-J, Li C-X, Gu G-Y, Zhu L-M. Modeling and compensating the dynamic hysteresis of piezoelectric actuators via a modified rate-dependent Prandtl–Ishlinskii model. Smart Mater Struct 2015;24(12):125006. http://dx.doi.org/10.1088/0964-1726/24/12/125006.

[23] Qin Y, Tian Y, Zhang D, Shirinzadeh B, Fatikow S. A novel direct inverse modeling approach for hysteresis compensation of piezoelectric actuator in feedforward applications. IEEE/ASME Trans Mechatronics 2013;18(3):981–9. http://dx.doi.org/10.1109/TMECH.2012.2194301.

[24] Furutani K, Urushibata M, Mohri N. Displacement control of piezoelectric element by feedback of induced charge. Nanotechnology 1998;9(2):93–8. http://dx.doi.org/10.1088/0957-4484/9/2/009.

[25] Ronkanen P, Kallio P, Koivo H. Current control of piezoelectric actuators with power loss compensation. In: IEEE/RSJ international conference on intelligent robots and system, vol. 2, (October):IEEE; 2002, p. 1948–53. http://dx.doi.org/10.1109/IRDS.2002.1044041, URL http://ieeexplore.ieee.org/document/1044041/.

[26] Gan J, Zhang X. A review of nonlinear hysteresis modeling and control of piezoelectric actuators. AIP Adv 2019;9(4). http://dx.doi.org/10.1063/1.5093000.

[27] Gu GY, Zhu LM, Su CY, DIng H, Fatikow S. Modeling and control of piezo-actuated nanopositioning stages: A survey. IEEE Trans Autom Sci Eng 2016;13(1):313–32. http://dx.doi.org/10.1109/TASE.2014.2352364.

[28] Pei J-S. Mem-spring models combined with hybrid dynamical system approach to represent material behavior. J Eng Mech 2018;144(12):4018109.

[29] Fang D, Liu J. Basic equations of piezoelectric materials. In: Fracture mechanics of piezoelectric and ferroelectric solids. Berlin, Heidelberg: Springer Berlin Heidelberg; 2013, p. 77–95.

[30] Ramberg W, Osgood WR. Description of stress-strain curves by three parameters. Natl Advis Comm Aeronaut 1943. Technical Note No. 902.
[31] Rasmussen C, Williams C. Gaussian processes for machine learning. London, England: MIT Press; 2006, http://dx.doi.org/10.1142/S0129065704001899.
[32] Nocedal J, Wright SJ. Numerical optimization. In: Springer series in operations research and financial engineering, New York: Springer-Verlag; 1999, http://dx.doi.org/10.1007/b98874.
[33] Boeren F, Bareja A, Kok T, Oomen T. Frequency-domain ILC approach for repeating and varying tasks: With application to semiconductor bonding equipment. IEEE/ASME Trans Mechatronics 2016;21(6):2716–27. http://dx.doi.org/10.1109/TMECH.2016.2577139.
[34] Pintelon R, Schoukens J. System identification: A frequency domain approach. second ed.. Wiley; 2012, p. 787. http://dx.doi.org/10.1002/0471723134.
[35] Oomen T, Rojas CR. Sparse iterative learning control with application to a wafer stage: Achieving performance, resource efficiency, and task flexibility. Mechatronics 2017;47:134–47.
[36] Norrlöf M, Gunnarsson S. Time and frequency domain convergence properties in iterative learning control. Internat J Control 2002;75(14):1114–26. http://dx.doi.org/10.1080/00207170210159122.

**Max van Meer** received his M.Sc. degree (cum laude) in mechanical engineering from the Eindhoven University of Technology, Eindhoven, the Netherlands, in 2021, where he is currently pursuing a Ph.D. degree in the Control Systems Technology section. His research interests include machine learning for control, and data-driven calibration of sensors and actuators.

**Tim van Meijel** received his M.Sc. degree (cum laude) in mechanical engineering from the Eindhoven University of Technology, Eindhoven, the Netherlands, in 2024.

**Emile van Halsema** is Mechatronics Engineer at Thermo Fisher Scientific, Eindhoven, the Netherlands. He received his M.Sc. degree in mechanical engineering from the Eindhoven University of Technology, Eindhoven, the Netherlands, in 2017.

**Edwin Verschueren** is Senior Mechatronics Engineer at Thermo Fisher Scientific within the Materials and Structural Analysis division. He holds the position of competence owner on mechatronic systems design. He received his M.Sc. degree in 1996 from Eindhoven University of Technology, Eindhoven and started working for ASML as mechatronics engineer. He continued his profession from 2001 until now at Thermo Fisher Scientific (formerly FEI Company) and during his career he was responsible for the design and market introduction of mechatronic modules for electron microscopes (sample manipulation stages, apertures mechanisms and sample loaders). Key aspects of his work are evaluation and integration of innovative technologies into solutions for high precision sample manipulation. His interests are in the field of physical modeling, actuator and sensor technologies and control algorithm design.

**Gert Witvoet** received the M.Sc. (cum laude) and Ph.D. degrees from the Eindhoven University of Technology, Eindhoven, The Netherlands, in 2007 and 2011, respectively. He is currently a Senior Dynamics and Control Specialist at the Netherlands Organization for Applied Scientific Research (TNO), Delft, The Netherlands, and a part-time Associate Professor with the Mechanical Engineering Department, Eindhoven University of Technology. His research interest includes the application of advanced motion control techniques on high-tech instruments and applications in the semiconductor, astronomy, and space markets. Dr. Witvoet is a recipient of the Unilever Research Prize and several best master teacher awards.

**Tom Oomen** is full professor with the Department of Mechanical Engineering at the Eindhoven University of Technology. He is also a part-time full professor with the Delft University of Technology. He received the M.Sc. degree (cum laude) and Ph.D. degree from the Eindhoven University of Technology, Eindhoven, The Netherlands. He held visiting positions at KTH, Stockholm, Sweden, and at The University of Newcastle, Australia. He is a recipient of the 7th Grand Nagamori Award, the Corus Young Talent Graduation Award, the IFAC 2019 TC 4.2 Mechatronics Young Research Award, the 2015 IEEE Transactions on Control Systems Technology Outstanding Paper Award, the 2017 IFAC Mechatronics Best Paper Award, the 2019 IEEJ Journal of Industry Applications Best Paper Award, and recipient of a Veni and Vidi personal grant. He is currently a Senior Editor of IEEE Control Systems Letters (L-CSS) and Co-Editor-in-Chief of IFAC Mechatronics, and he has served on the editorial board of IEEE Transactions on Control Systems Technology. He has also been vice-chair for IFAC TC 4.2 and a member of the Eindhoven Young Academy of Engineering. His research interests are in the field of data-driven modeling, learning, and control, with applications in precision mechatronics.